

# Map Optical Properties to Subwavelength Structures Directly via a Diffusion Model

Shijie Rao, Kaiyu Cui\*, Yidong Huang\*, Jiawei Yang, Yali Li,  
Shengjin Wang, Xue Feng, Fang Liu, and Wei Zhang

\* Correspondent author: [kaiyucui@tsinghua.edu.cn](mailto:kaiyucui@tsinghua.edu.cn),

[yidonghuang@tsinghua.edu.cn](mailto:yidonghuang@tsinghua.edu.cn)

Affiliation: Department of Electronic Engineering, Beijing National  
Research Center for Information Science and Technology (BNRist),  
Tsinghua University, Beijing, China

## Abstract

Subwavelength photonic structures and metamaterials provide revolutionary approaches for controlling light. The inverse design methods proposed for these subwavelength structures are vital to the development of new photonic devices. However, most of the existing inverse design methods cannot realize direct mapping from optical properties to photonic structures but instead rely on forward simulation methods to perform iterative optimization. In this work, we exploit the powerful generative abilities of artificial intelligence (AI) and propose a practical inverse design method based on latent diffusion models. Our method maps directly the optical properties to structures without the requirement of forward simulation and iterative optimization. Here, the given optical properties can work as “prompts” and guide the constructed model to correctly “draw” the required photonic structures. Experiments show that our direct mapping-based inverse design method can generate subwavelength photonic structures at high fidelity while following the given optical properties. This may change the method used for optical design and greatly accelerate the research on new photonic devices.

## Introduction

Subwavelength structures such as photonic crystals and metamaterials have led to revolutionary approaches for light field regulation<sup>1</sup>. The derived photonic devices can realize incredible features such as negative refractive index<sup>2,3</sup>, complete photonic bandgaps<sup>4</sup>, complex dispersion functions<sup>5</sup>, etc. Due to these subwavelength structures cannot be analytically modelled by geometric optics or wave optics, they face various difficulties in tailoring. Conventional forward design approaches mainly achieved by choosing an optimal match from a predefined library<sup>6-9</sup> of photonic structures, while with limited degrees of design freedom, such an insufficient design space. The lack of accurate and accelerated design methods has become a major concern regarding the further development of new photonic devices<sup>10</sup>.

The newly developed inverse design approaches provide solutions that overcome the limitations of predefined libraries<sup>11-13</sup>. They can greatly enlarge the design space and have shown powerful capabilities for generating less intuitive but more effective photonic structures. Unlike forward design methods, inverse design strategies need not rely on any predefined libraries and usually transform an inverse design problem into an optimization problem to obtain the optimal design by iterative algorithms<sup>14-23</sup> instead. However, in each iteration of optimization, the generated photonic structure needs to be forward modeled to get the optical responses and calculate the objective function. The lack of analytical models makes forward modeling generally performed by numerical simulation methods such as the finite-difference time-domain (FDTD)<sup>24</sup>, which is computationally expensive. Besides, the current inverse design methods potentially face the common problems encountered by optimization algorithms involving convergence, efficiency, and global optima. They hardly realize an inverse mapping of forward modeling. If a direct mapping from optical properties to photonic structures can be established, we can break the limitations of optimization algorithms and discard the requirement of computationally expensive simulation.

Unfortunately, achieving such a direct mapping faces many problems like as the non-uniqueness or existence of solutions, and the fabrication constraints<sup>1</sup>. As is difficult

to develop a universal mathematical analytic model, several attempts have been made to train deep neural networks (DNNs) to achieve a direct mapping in a predefined and limited design space where the inverse problem is a one-to-one mapping<sup>25-30</sup>. Other attempts adopt generative DNNs to solve the problem of non-uniqueness and enlarge the design space<sup>31-36</sup>. These methods have shown incredible abilities, but they still face some common challenges due to the direct mapping-based inverse design process itself and the limitations of DNNs. The first issue is that the solution of one specific inverse design problem may be non-unique, or may not exist. It is hard to design and train a DNN to fit a one-to-many or one-to-none mapping function. Second, training dataset needs to be carefully designed because it defines the search space. It is expected to contain arbitrary photonic structures that meet the fabrication constraints rather than structures only generated from some predefined parameters. Finally, the acceptable input optical properties are limited. During the training process, the optical properties are usually acquired directly via forward prediction and fed to the network as inputs. In this way, the trained DNN may only accept the whole realistic optical properties as inputs, which is not practical and user-friendly. Therefore, realizing a practical direct mapping-based inverse design method still requires overcoming several difficulties.

Recent research on artificial intelligence (AI)-generated content<sup>37</sup> and AI for science have shown great potential of DNNs in various practical fields, such as the generation of realistic images<sup>38-40</sup>, chatbots<sup>41,42</sup>, medicine<sup>43,44</sup>, chemical research<sup>45</sup>, and mechanical research<sup>46</sup>. Among these models, text-to-image denoising diffusion models are especially suitable for direct mapping-based inverse design tasks. In this paper, we present an inverse design method to achieve direct mapping from optical properties to photonic structures based on latent diffusion model<sup>39</sup>, the developed approach is called artificial intelligence-generated photonic structures (AIGPS). Here, the given optical properties can work as “text prompts” and guide the model to “draw” the required photonic structures. To achieve such a direct mapping, we devise an encoding method of optical properties and design a prompt encoder network to work together with the diffusion model to solve the non-uniqueness problem and provide a user-friendly interface for inputting optical properties. The diffusion model can offer improved image

synthesis ability compared with other generative DNNs<sup>47-49</sup> and we utilize the strong generative capabilities of diffusion model to enlarge the search space and design new photonic structures. Also, a fast forward prediction network is proposed to provide a full deep learning approach and realize effective training. Besides, we present a training dataset containing arbitrary shapes, which empowers as large design space as possible while meeting fabrication limits. As new photonic devices are generally composed of individual subwavelength structures or arrays of building blocks which are usually referred to as meta-atoms<sup>6,7,50-52</sup>, we illustrate the powerful direct mapping capabilities of our method with the example of designing meta-atoms from a given transmission property. Moreover, our method can be easily generalized to other inverse design problems via transfer learning.

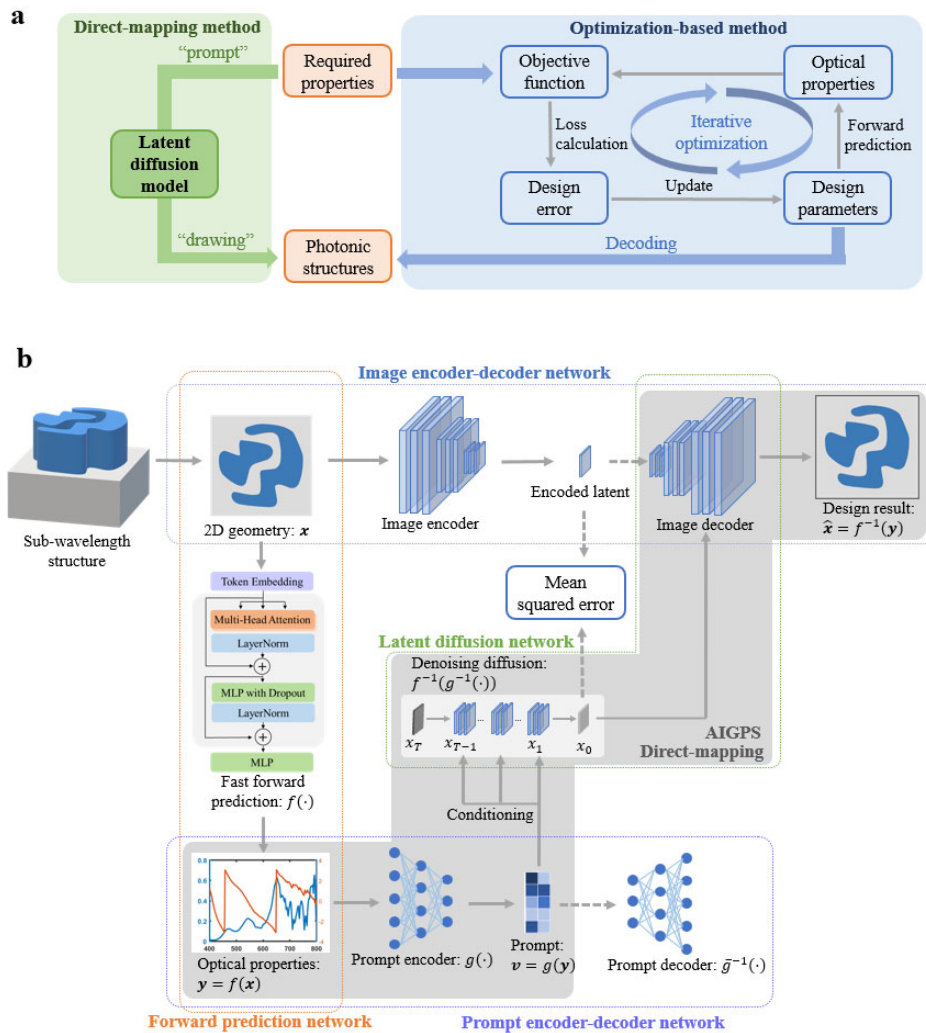


**Fig. 1 Schematics of inverse design methods. a, Optimization-based inverse**

design methods usually model only the forward prediction process and execute iterative optimization algorithms to obtain an inverse design result. Instead, direct mapping-based inverse design methods aim at modeling the inverse problem of forward prediction directly. **b**, The framework of our proposed direct-mapping inverse design method is based on latent diffusion. It mainly consists of an image encoder-decoder network (MLP: multilayer perceptron), a forward prediction network, a prompt encoder-decoder network, and a latent diffusion network. Note that only the image decoder, prompt encoder, and latent diffusion are needed at inference.

## Results

### Inverse design via a latent diffusion model

Assuming that the given photonic structure is  $x$  and the corresponding optical property is  $y$ , optimization-based inverse design methods model the forward prediction process  $f(\cdot)$  such that  $y = f(x)$  and perform the inverse design procedure by solving the optimization problem  $\hat{x} = \underset{z}{\text{minimize}} ||y - f(z)||$ . As shown in Fig. 1a, the optimization process usually requires iterative calculations. Instead, the direct mapping-based inverse design method attempts to model the inverse function of  $f(\cdot)$  such that we can directly obtain the inverse design result  $\hat{x} = f^{-1}(y)$  without any iteration. Our implementation for obtaining such an inverse function is shown in Fig. 1b. A subwavelength structure can be described by its geometry, and this geometry is usually parameterized by binary-valued pixels that indicate different materials, such as silicon and air. To accelerate the diffusion process and reduce the number of required network parameters, we adopt the latent diffusion<sup>39</sup> strategy, which encodes the target geometry to a set of latent parameters to greatly reduce the dimensionality of the design parameters and conduct the diffusion process in the latent space. The latent parameters generated by the diffusion network are finally decoded by the image decoder network to obtain the design results. The implementation details of our diffusion network and image encoder-decoder network are described in the Methods section.

As shown in Fig. 1b, in addition to the latent diffusion network and image encoder-

decoder network, an additional forward prediction network and a prompt encoder-decoder network are also included in our inverse design framework. Although forward prediction is not needed in the direct mapping-based inverse design process, it is required during the training process to generate the input data. Therefore, to accelerate the forward prediction process, we propose a DNN-based forward prediction network to replace the numerical simulation method and efficiently train the diffusion network.

The prompt encoder network is proposed to perform fuzzy searches because we cannot find a photonic structure that exactly matches the given optical property, but we try to find compatible solutions in most cases. The prompt encoder network is trained to encode only the required key features of the input optical properties while ignoring other irrelevant details via self-supervised learning. The encoded results work as conditional controls for the diffusion process and guide the diffusion network to generate subwavelength structures that match the required key features. To be more specific, assuming that the prompt encoder network is  $g(\cdot)$ , its output  $v = g(y)$  indicates the reduced properties that contain only key features such as the working band, cutoff frequency, and resonance point. In this way, the diffusion network is not trained to model  $\hat{x} = f^{-1}(y)$  but rather to model  $\hat{x} = f^{-1}(g^{-1}(v))$ . Notably,  $v = g(y)$  is a many-to-one mapping because optical properties such as the transmission responses of different meta-atoms can have the same key features. Therefore, by learning the one-to-many mapping function  $g^{-1}(\cdot)$ , our inverse design method can solve the nonuniqueness problem. Moreover, we can send only the key features instead of the whole accurate optical property to the inverse design algorithm. The prompt encoder network can accept abstract inputs, which enables fuzzy searches and provides a user-friendly interface. Our method is a data-driven approach, and the input training dataset is vital to the performance of our inverse design method because it determines the search space. Therefore, the training dataset is expected to contain 2D geometries that are as arbitrary as possible. Referring to the freeform shape generation method<sup>53</sup>, we design an algorithm to build a dataset of arbitrary shapes that satisfies the imposed fabrication limits. These arbitrary shapes provide a much larger design space than do shapes generated from predefined parameters, thus enabling the inverse design of

subwavelength structures with complex functions.

The principles and capabilities of our inverse method are introduced via a meta-atom design example in this paper. Silicon meta-atoms are widely adopted in metasurfaces with various functions<sup>6,17,50,52,54</sup>. Therefore, we take meta-atoms based on a silicon-on-insulator (SOI) with a 220-nanometer-thick silicon layer as an example and train the network to produce an inverse design subjected to the given transmission response. We also show that our inverse design method can be easily converted to design meta-atoms based on other materials, such as the commonly used 600-nanometer-thick TiO<sub>2</sub> layers on SiO<sub>2</sub> substrates. The detailed results obtained concerning the inverse TiO<sub>2</sub> meta-atom design process can be found in Supplementary Note 1. As numerical simulations are time-consuming, by using only a small number of simulated meta-atoms as training samples, the transmission properties of every meta-atom can be quickly and accurately predicted by the designed forward prediction network. Note that although our inverse design method contains several different networks, which will be further introduced in the following sections, only the image decoder network, prompt encoder network, and latent diffusion network are needed for inference purposes. The training protocol can be found in the Methods section.

### **Forward prediction network based on a transformer model**

Our forward prediction network builds on the vision transformer<sup>55</sup> model. We slice the 2D geometry of the target meta-atom into  $16 \times 16$  patches, and this strategy is similar to the mesh process in an FDTD simulation. Each patch works as an input token of the transformer. The period of the meta-atom is randomly chosen from 300 nm to 700 nm and attached to the end of the token sequence, as shown in Fig. 2a. Other network details are described in Supplementary Note 2. The network predicts the complex-valued transmission response of the meta-atom under horizontally polarized incident light. It is trained to be a polarization-sensitive structure. To predict the transmission response generated under vertically polarized incident light, we can simply rotate the geometry of the meta-atom by 90 degrees and conduct prediction again using the same forward prediction network. The network outputs the real and

imaginary parts of the complex-valued transmission response, which can be further converted to the transmission power spectrum and phase spectrum.

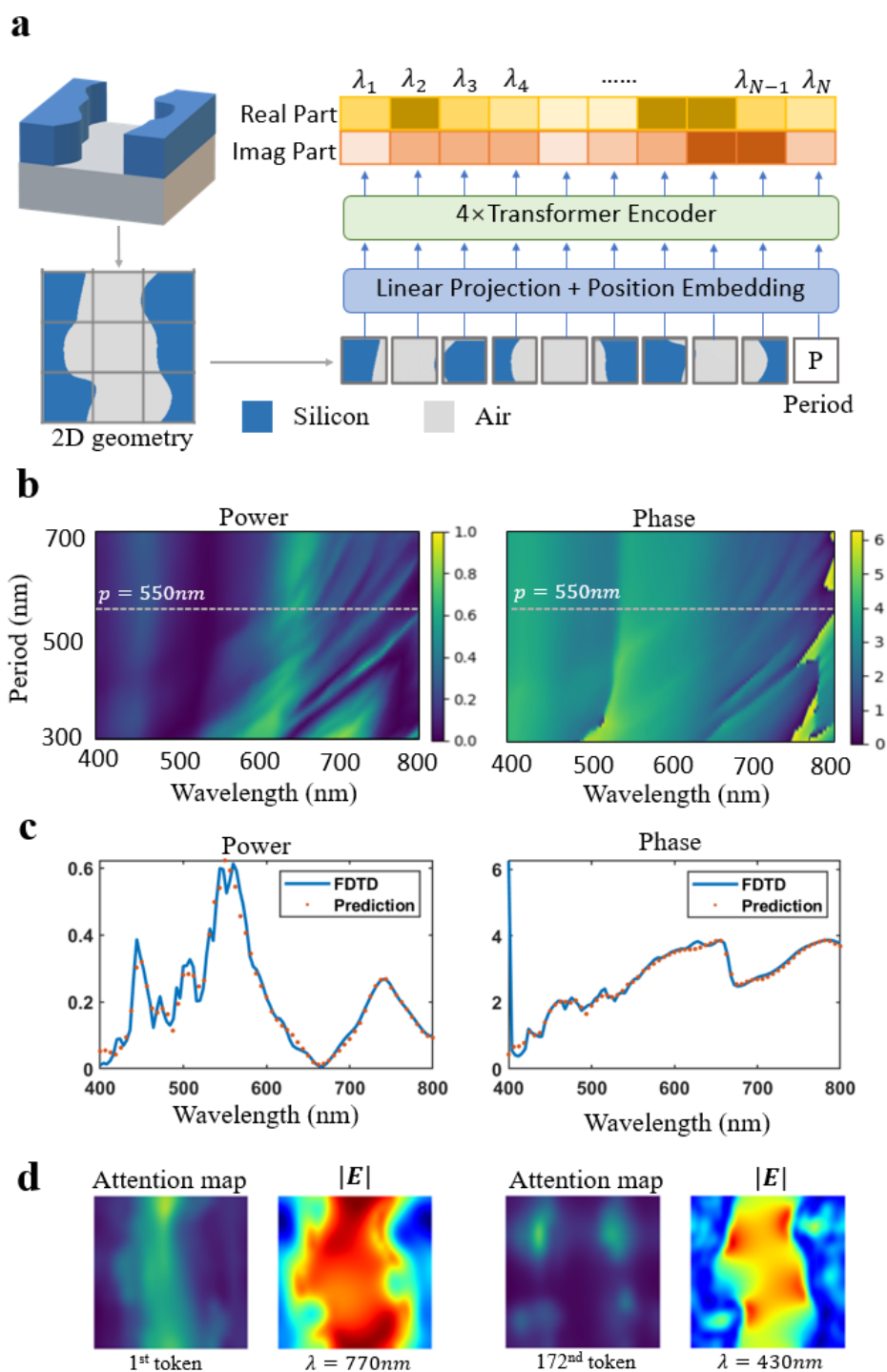


**Fig. 2** The forward prediction network and its prediction results. **a.** The network is based on the vision transformer model. The 2D geometry of the meta-atom is sliced into several patches and sent to the network as inputs; this strategy is similar to the mesh process in FDTD simulations. The period of the meta-atom is also taken as



an input. **b.** The predicted transmission power and phase responses of the meta-atom are shown in **a.** We sweep the period parameter from 300 nm to 700 nm. **c.** This subfigure shows the predicted results obtained with a period  $p = 550\text{nm}$ , which are marked as gray dashed lines in **b.** The prediction fits well with the FDTD simulation results. **d.** The attention maps of the transformer block display some similarities to the electric field distribution at several wavelengths.

To study the performance of our forward prediction network, we employ it in a parameter sweeping task. Parameter sweeps are commonly utilized in meta-atom design tasks to find the optimal design parameter. We sweep the period of the meta-atom shown in Fig. 2a from 300 nm to 700 nm. The transmission power spectrum and phase spectrum predicted by our network under different periods are shown in Fig. 2b. We also present the prediction results obtained with a period  $p = 550\text{nm}$  separately in Fig. 2c for comparison with the FDTD simulation results. The network predictions and simulation results are almost identical. A quantitative analysis reveals that the mean squared error and cosine similarities between the results of our network and the FDTD simulation on the testing dataset are approximately 0.040 and 98.2%, respectively. Additional testing results can be found in Supplementary Note 3. However, our network can complete the calculation process in 4 seconds, while the FDTD simulation procedure requires more than 2 hours on the same CPU device (an Intel Core i7-11700 CPU @ 2.50 GHz). The proposed method is approximately 2000 times faster than the FDTD simulation strategy and can be even faster when accelerated by a GPU.

After training, the forward prediction network is fixed for training the diffusion network. Its performance indicates great potential for quickly obtaining the transmission responses of meta-atoms. Similar DNN-based fast forward prediction strategies have been adopted in previous works<sup>22,25,28,56</sup>. However, the existing approaches usually take some predefined parameters, such as the radius and width, as inputs. In this way, the constructed DNN can only be applied to certain regular geometries. Our prediction network is designed to perform forward prediction for arbitrary shapes. It does not make any assumptions about the geometries of the

subwavelength structures, thus attaining better generalizability. This method can be an alternative and efficient tool for replacing numerical simulation in studies involving metasurfaces and subwavelength structures. Furthermore, our forward prediction network has four transformer blocks, and each block can output an attention map generated by the self-attention mechanism. Analyzing these attention maps provides a possible way to understand a black-box DNN model. For example, by studying the attention maps produced by our network, we find that the first transformer block mainly extracts the interrelationships between contiguous patches, which is comprehensible because the light field is usually localized in subwavelength structures. The second block attempts to analyze the interactions between nonadjacent patches, which may help when studying nonlocal light fields. The second attention map exhibits some similarities to the electrical field distribution under certain wavelengths, as shown in Fig. 2d. The attention maps are further analyzed in Supplementary Note 4.

### **Prompt encoder network trained by self-supervised learning**

As mentioned above, a prompt encoder network is vital for solving the nonuniqueness problem. We propose a self-supervised learning strategy inspired by masked autoencoders<sup>57</sup> to train a network that satisfies these requirements. As shown in Fig. 3a, the input of the prompt encoder network is the masking property, which is acquired by applying a certain mask to the input. In this way, some spectral bands of the transmission response are masked (where  $mask = 0$ ) and unseen by the network. Only the unmasked (where  $mask = 1$ ) bands are accepted by the network and encoded. Utilizing this strategy, we can mask the insignificant parts of the optical properties of interest and guide the prompt encoder network to output the reduced key features rather than the entire set of precise features.

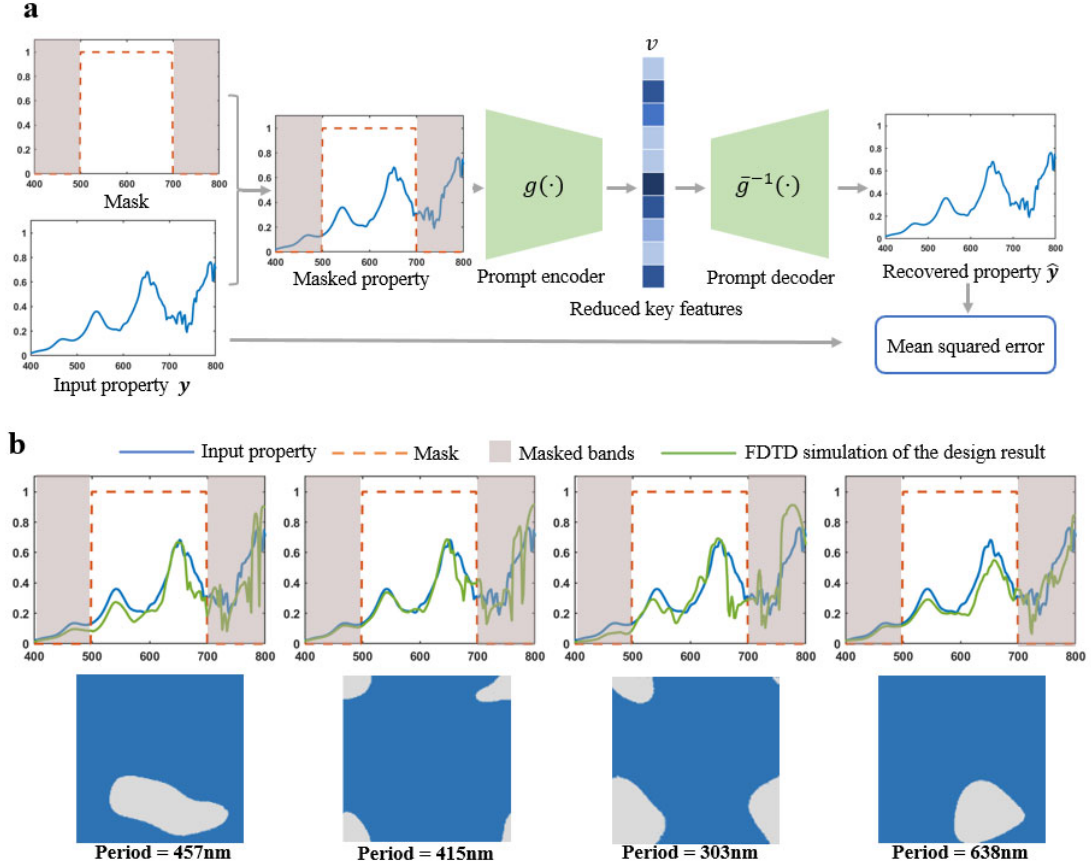


**Fig. 3 Schematic of the prompt encoder network.** **a.** The inputs of the prompt encoder network include the target optical property and a mask. Only the unmasked part of the property is seen by the network. An additional prompt decoder network is adopted to train the prompt encoder network via self-supervised learning. **b.** Different inverse design results that are subject to the same input property and mask are shown in **a**. The proposed prompt encoder empowers such a one-to-many mapping to solve the nonuniqueness problem.

To train a high-performance prompt encoder network, we need another decoder network that can enable self-supervised learning. The decoder network  $\bar{g}^{-1}(\cdot)$  tries to recover the entire precise property according to the reduced key features  $v$ . Here,  $\bar{g}^{-1}(\cdot)$  is designed to be a one-to-one mapping rather than a one-to-many mapping to ensure the uniqueness of its output. Self-supervised learning can be achieved by minimizing the mean squared error between the one-to-one pairs of the input property  $y$  and the recovered property  $\bar{y}$ . The detailed training strategy and network

architecture are listed in Supplementary Note 5. The training dataset includes some realistic transmission responses simulated by FDTD and some handcrafted transmission responses, including some ideal filter responses, resonance peaks, and random Fourier and Gaussian curves. In this way, we train the prompt encoder to accept both realistic data and abstract data. After conducted self-supervised learning, the decoder network is discarded, and the encoder network is fixed for training the diffusion network. Given the design target (the input property and mask) shown in Fig. 3a, after performing encoding through the prompt encoder network, the latent diffusion network can be guided to generate various design results (Fig. 3b). Each result presents a possible solution to the inverse design problem, indicating that the proposed prompt encoder enables a one-to-many mapping to solve the nonuniqueness problem.

### **Inverse design results produced by the diffusion network**

After preparing the forward prediction network and the prompt encoder network, the diffusion network can be effectively trained. To test its direct mapping-based inverse design ability, we first attempt to map a full-band precise realistic transmission power response to its corresponding meta-atom, as shown in Fig. 4a. The 2D geometry and period of the meta-atom are generated directly by the diffusion network, and forward prediction is not needed. We simulate the transmission responses of the generated meta-atoms via FDTD, and they are displayed as green curves. The simulated transmission responses fit well with the design target. The results indicate great inverse design performance. Fig. 4b displays the working process of the latent diffusion network. After several denoising and diffusion steps, the required meta-atom is directly generated to not only satisfy the given transmission power properties but also meet the imposed fabrication requirements. Notably, some delicate structures that are too small to fabricate are automatically eliminated because our training dataset is designed to ensure that the generated shapes satisfy the required fabrication constraints.

C4 symmetry is an important property because meta-atoms with C4 symmetry are polarization-insensitive<sup>50</sup>. Our diffusion network can also be controlled to generate meta-atoms with or without C4 symmetry constraints. Fig. 4c shows the inverse design

of a meta-atom with C4 symmetry. The design results also meet expectations. In addition, we can mask some uninteresting bands and generate meta-atoms that satisfy the given transmission power properties in a certain band. Some examples are shown in Fig. 4d and Fig. 4e. These results indicate that the masking strategy and the prompt encoder network provide a flexible format for the input design target.

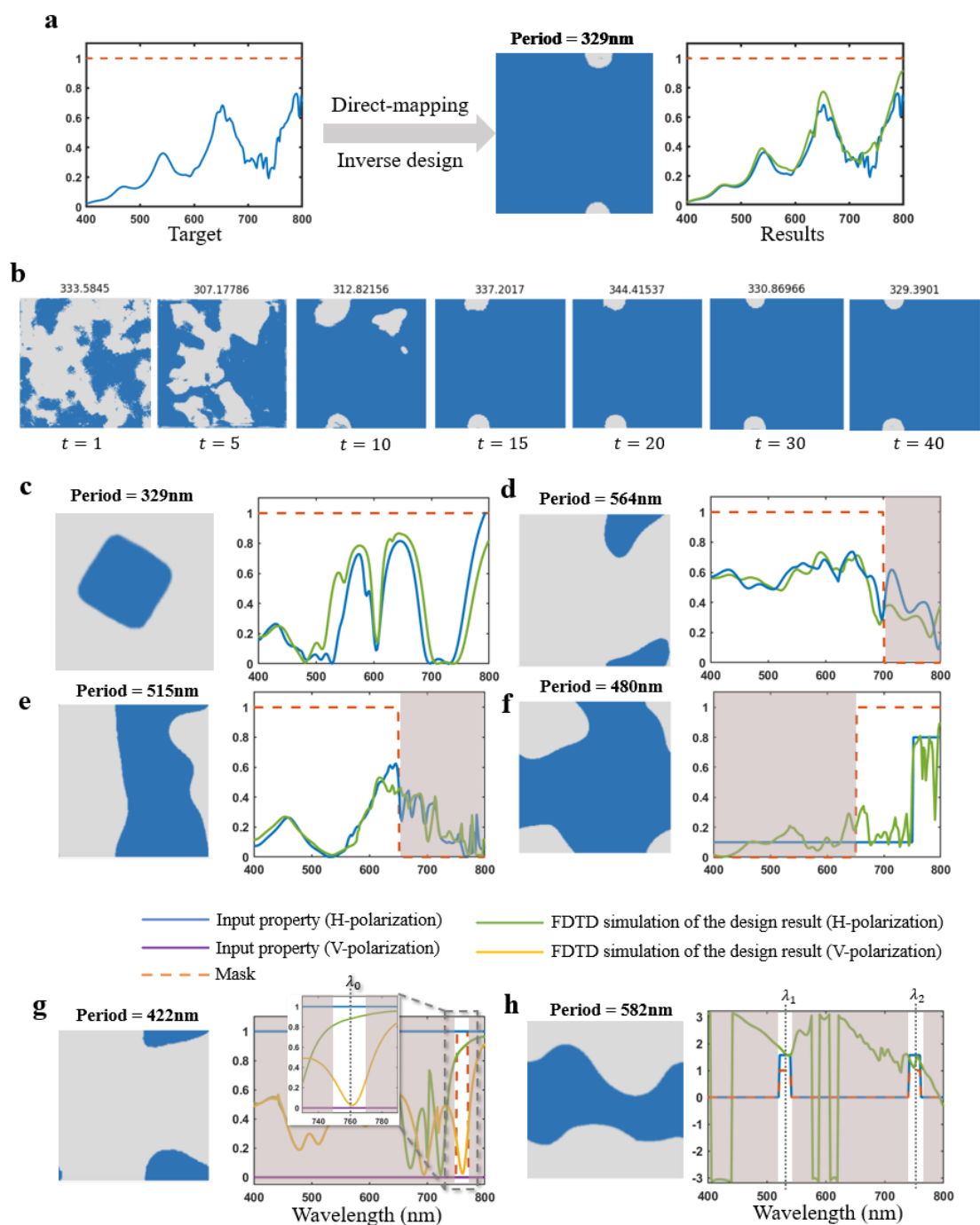


**Fig. 4 Inverse design results.** **a.** A full-band precise realistic transmission power response is used as the design target. **b.** The working process of the latent diffusion

network. The required meta-atom is directly generated after a few denoising and diffusion steps. **c-f.** Examples of meta-atoms that are inversely designed according to the given transmission responses. **g.** Examples of inversely designed meta-atoms produced according to the transmission responses induced under different polarization conditions. **h.** An example of an inversely designed meta-atom constructed according to the transmission phase responses.

More generally, we do not fully know the precise transmission power response. Instead, we can only provide some abstract design parameters. Fig. 4f shows such an example of designing a longwave pass filter. The cutoff wavelength is expected to be approximately 750 nm, and the working band is 650~800 nm. These specifications can be easily converted to the input property (blue curve) and the input mask (orange curve) shown in Fig. 4f, which can be accepted by the prompt encoder network. Then, we can obtain the inverse design result, which is also shown in Fig. 4e. The result indicates the fuzzy search ability of our inverse design method. Such an ideal filter cannot be achieved by a 220-nanometer-thick silicon meta-atom. However, our diffusion network attempts to generate solutions that satisfy the requirements to the greatest extent possible. The performance of the meta-atom generated by our method is also verified by an FDTD simulation. In addition to mapping the transmission power spectrum to the meta-atom, we also achieve direct mapping from the polarization properties or transmission phase spectrum to the meta-atom. Fig. 4g shows an example in which we design a meta-atom that has high-power transmission for horizontally polarized light and low-power transmission for vertically polarized light at a certain wavelength  $\lambda_0$ . Such an inverse design ability can be utilized to design a polarizer or a polarization beam splitter. Fig. 4h shows another example of designing a meta-atom that produces the same transmission responses at two different wavelengths  $\lambda_1$  and  $\lambda_2$ ; this is useful for designing phase modulation devices that work at multiple wavelengths. These results indicate the great potential of our inverse design method for use in various applications. More technical analysis regarding the latent diffusion network can be found in Supplementary Note 6.

## Discussion

We propose a direct mapping-based inverse design method named AIGPS based on a diffusion model. While most of the existing inverse design methods are based on combinations of optimization algorithms and forward prediction strategies, our inverse design achieves direct mappings from optical properties to photonic structures, indeed providing the inverse function of forward prediction. Powered by this direct mapping technique, our method realizes a fast inverse design process without forward prediction and iterative optimization requirements. Moreover, our inverse design method is more practical than other approaches because it provides a user-friendly interface for accepting abstract design parameters as inputs rather than a whole precise optical property.

One of the greatest difficulties encountered when utilizing such a direct mapping-based inverse design is the uncertainty of the solution: the solution may not be unique or may not even exist. If the solution does not exist, our method attempts to design a structure that satisfies the requirements to the greatest extent possible via a fuzzy search. However, if the given property is completely impossible to realize and no close solution can be obtained, such as in the design of a 220-nanometer-thick silicon meta-atom with high transmission at approximately 400 nm, the diffusion network may generate some random outputs because the training dataset does not contain such an impossible matching; therefore, the network does not learn to map such an input. Fortunately, our forward prediction network can be utilized to quickly evaluate the produced inverse design results. Therefore, we can determine the confidence of the inverse design results without further simulation.

In this work, we focus on inversely designing meta-atoms. Although meta-atoms have wide applications in various photonic devices, they are relatively small-scale photonic structure units and are usually studied under periodic boundary conditions. Other photonic devices, such as high-performance metalenses, require the design of very large-scale photonic structures to overcome the limits of periodic meta-atoms. Our

method still has the potential to solve such a large-scale inverse design problem because these large-scale structures can also be described by their geometries and compressed by the image encoder network to reduce the number of required design parameters. Latent diffusion models are also efficient at generating large-scale images. The greatest challenge is how to obtain an appropriate training dataset because the simulation of these large-scale structures requires considerable computational resources, and the dataset should contain many more samples due to the significant expansion of the design space. To solve this problem, our future work will first focus on forming a fast forward prediction method for large-scale photonic structures. Physics-informed neural networks (PINNs) may be viable for reducing the training dataset requirements. The powerful abilities of pretrained large language models (LLMs) can also be exploited to help develop photonic techniques.

## **Methods**

### **Implementation of the Latent Diffusion Network**

The overall architecture of our denoising diffusion model builds on the latent diffusion model (LDM)<sup>39</sup>. We make some modifications and improvements so that the LDM is suitable for generating meta-atoms with limited training data, and we adopt the TensorFlow<sup>58</sup> framework to implement all of the DNN models. Here, we briefly introduce our denoising diffusion model, and more technical details can be found in the ‘Code availability’ section. First, the 2D geometry of the target meta-atom is described by a binary image with a size of  $256 \times 256$ . The period of the meta-atom is normalized to the range of  $(0, 1]$  and multiplied by the binary image. The image encoder-decoder network is based on a CNN with residual connections and a self-attention mechanism. The image encoder/decoder can encode/decode the image to/from the latent space with a size of  $32 \times 32 \times 2$ . Denoising diffusion is conducted in the latent space to greatly reduce the incurred computational cost. The diffusion network is based on the U-Net architecture with cross-attention to introduce conditional control. The sampling strategy used in our diffusion process is DDIM<sup>49</sup>, and we adopt a continuous diffusion time,



which embeds the noise rate and signal rate into the diffusion network. In this way, the number of sampling steps can be dynamically changed at inference time. In our experiments, we find that 20 steps are sufficient for effectively generating the required meta-atom.

### **Freeform meta-atom generation and simulation**

The training dataset directly determines the search space of the diffusion network. It is vital for training a high-performance inverse design model and ensuring that the subwavelength structures generated by the diffusion network satisfy the imposed fabrication limits. We generate approximately 200 thousand shapes as arbitrarily as possible with and without the  $C_4$  symmetry constraint. The shapes are then randomly split into training and testing sets at a ratio of 9 to 1. The periods of the meta-atoms are between 300 nm and 700 nm. The minimum curvature radius of the shapes is restricted to 45 nm to meet the fabrication limit. If we sample the period at 10 nm intervals from 300 nm to 700 nm, we obtain 41 different values. We combine these period values with 200 thousand different shapes and obtain approximately  $10^7$  different meta-atoms. It is difficult to simulate all of these meta-atoms via numerical simulation. Therefore, we only simulate approximately  $10^5$  meta-atoms to train the forward prediction network. The simulation process is performed by the FDTD method under periodic boundary conditions and horizontally polarized incident light. The transmission responses of the other meta-atoms are then quickly predicted.

### **Training and inference protocols**

Each meta-atom is described by a  $256 \times 256$  image. The values of the pixels are normalized to  $[-1, 1]$ . The image is encoded in a  $32 \times 32 \times 2$  latent space by the image encoder, and the latent space is then normalized to a mean of 0 and a variance of 1. Then, we can train the image encoder-decoder network. The forward prediction network takes a binary image representing the 2D geometry and the period value separately as inputs rather than encoding them to form a single image. The image encoder-decoder network and forward prediction network are first trained. Then, all of

the transmission responses of the meta-atoms can be predicted quickly via forward prediction, and these responses can be used as the training set to train the prompt encoder network. Finally, we fix the trained image encoder network, forward prediction network, and prompt encoder network and train the diffusion network. At each training step, a batch of shapes is randomly chosen from the training set, and for each shape, we randomly generate a period value to form a meta-atom. Then, the transmission responses are predicted, and the meta-atoms are encoded in the latent space. The transmission responses are further encoded by the prompt encoder network and used as a conditional control mechanism for the diffusion network. Finally, we train the diffusion network to denoise the latent space with guidance provided by the input conditional control and the signal-to-noise ratio. All of the networks are trained by the Adam<sup>59</sup> optimizer with a weight decay rate of 0.0001, and the loss is calculated as the mean squared error. At inference time, only the image decoder network, prompt encoder network, and diffusion network are necessary. However, we can also use the forward prediction network to evaluate the generated results.

## Funding

This work is supported by the National Key Research and Development Program of China (2023YFB2806703, 2022YFF1501600). The National Natural Science Foundation of China (Grant No. U22A6004); Beijing Frontier Science Center for Quantum Information; and Beijing Academy of Quantum Information Sciences.

## References

- 1 Ma, W. *et al.* Deep learning for the design of photonic structures. *Nature Photonics* **15**, 77-90 (2021). <https://doi.org/10.1038/s41566-020-0685-y>
- 2 Smith, D. R., Pendry, J. B. & Wiltshire, M. C. K. Metamaterials and Negative Refractive Index. *Science* **305**, 788-792 (2004). <https://doi.org/doi:10.1126/science.1096796>
- 3 Soukoulis, C. M., Linden, S. & Wegener, M. Negative Refractive Index at Optical Wavelengths. *Science* **315**, 47-49 (2007). <https://doi.org/doi:10.1126/science.1136481>
- 4 Cerjan, A. & Fan, S. Complete photonic band gaps in supercell photonic crystals.

*Physical Review A* **96** (2017). <https://doi.org/10.1103/physreva.96.051802>

5 Chen, W. T., Zhu, A. Y. & Capasso, F. Flat optics with dispersion-engineered metasurfaces. *Nature Reviews Materials* **5**, 604-620 (2020). <https://doi.org/10.1038/s41578-020-0203-3>

6 Khorasaninejad, M. *et al.* Metalenses at visible wavelengths: Diffraction-limited focusing and subwavelength resolution imaging. *Science* **352**, 1190-1194 (2016). <https://doi.org/doi:10.1126/science.aaf6644>

7 Miyata, M., Nemoto, N., Shikama, K., Kobayashi, F. & Hashimoto, T. Full-color-sorting metalenses for high-sensitivity image sensors. *Optica* **8**, 1596-1604 (2021). <https://doi.org/10.1364/OPTICA.444255>

8 Tian, T. *et al.* Metasurface-Based Free-Space Multi-Port Beam Splitter with Arbitrary Power Ratio. *Advanced Optical Materials* **11** (2023). <https://doi.org/10.1002/adom.202300664>

9 Chen, X. *et al.* All-Dielectric Metasurface-Based Beam Splitter with Arbitrary Splitting Ratio. *Nanomaterials* **11**, 1137 (2021). <https://doi.org/10.3390/nano11051137>

10 Li, Z., Pestourie, R., Lin, Z., Johnson, S. G. & Capasso, F. Empowering Metasurfaces with Inverse Design: Principles and Applications. *ACS Photonics* **9**, 2178-2192 (2022). <https://doi.org/10.1021/acsphotonics.1c01850>

11 Molesky, S. *et al.* Inverse design in nanophotonics. *Nature Photonics* **12**, 659-670 (2018). <https://doi.org/10.1038/s41566-018-0246-9>

12 Elsayy, M. M. R., Lanteri, S., Duvigneau, R., Fan, J. A. & Genevet, P. Numerical Optimization Methods for Metasurfaces. *Laser & Photonics Reviews* **14**, 1900445 (2020). <https://doi.org/10.1002/lpor.201900445>

13 Campbell, S. D. *et al.* Review of numerical optimization techniques for meta-device design [Invited]. *Optical Materials Express* **9**, 1842 (2019). <https://doi.org/10.1364/ome.9.001842>

14 Jensen, J. S. & Sigmund, O. Topology optimization for nano-photonics. *Laser & Photonics Reviews* **5**, 308-321 (2011). <https://doi.org/10.1002/lpor.201000014>

15 Fan, J. A. Freeform metasurface design based on topology optimization. *MRS Bulletin* **45**, 196-201 (2020). <https://doi.org/10.1557/mrs.2020.62>

16 Sell, D., Yang, J., Doshay, S., Yang, R. & Fan, J. A. Large-Angle, Multifunctional Metagratings Based on Freeform Multimode Geometries. *Nano Letters* **17**, 3752-3757 (2017). <https://doi.org/10.1021/acs.nanolett.7b01082>

17 Piggott, A. Y. *et al.* Inverse design and demonstration of a compact and broadband on-chip wavelength demultiplexer. *Nature Photonics* **9**, 374-377 (2015). <https://doi.org/10.1038/nphoton.2015.69>

18 Sui, S. *et al.* Symmetry-based coding method and synthesis topology optimization design of ultra-wideband polarization conversion metasurfaces. *Applied Physics Letters* **109**, 014104 (2016). <https://doi.org/10.1063/1.4955412>

19 Jafar-Zanjani, S., Inampudi, S. & Mosallaei, H. Adaptive Genetic Algorithm for Optical Metasurfaces Design. *Scientific Reports* **8**, 11040 (2018). <https://doi.org/10.1038/s41598-018-29275-z>

20 Jin, Z. *et al.* Complex Inverse Design of Meta-optics by Segmented Hierarchical Evolutionary Algorithm. *ACS Nano* **13**, 821-829 (2019).

<https://doi.org/10.1021/acsnano.8b08333>

- 21 Cai, H. *et al.* Inverse design of metasurfaces with non-local interactions. *npj Computational Materials* **6**, 116 (2020). <https://doi.org/10.1038/s41524-020-00369-5>
- 22 Inampudi, S. & Mosallaei, H. Neural network based design of metagratings. *Applied Physics Letters* **112**, 241102 (2018). <https://doi.org/10.1063/1.5033327>
- 23 Peurifoy, J. *et al.* Nanophotonic particle simulation and inverse design using artificial neural networks. *Science Advances* **4**, eaar4206 (2018). <https://doi.org/10.1126/sciadv.aar4206>
- 24 Teixeira, F. L. *et al.* Finite-difference time-domain methods. *Nature Reviews Methods Primers* **3** (2023). <https://doi.org/10.1038/s43586-023-00257-4>
- 25 An, S. *et al.* A Deep Learning Approach for Objective-Driven All-Dielectric Metasurface Design. *ACS Photonics* **6**, 3196-3207 (2019). <https://doi.org/10.1021/acsp Photonics.9b00966>
- 26 Malkiel, I. *et al.* Plasmonic nanostructure design and characterization via Deep Learning. *Light: Science & Applications* **7** (2018). <https://doi.org/10.1038/s41377-018-0060-7>
- 27 Ma, W., Cheng, F. & Liu, Y. Deep-Learning-Enabled On-Demand Design of Chiral Metamaterials. *ACS Nano* **12**, 6326-6334 (2018). <https://doi.org/10.1021/acsnano.8b03569>
- 28 Liu, D., Tan, Y., Khoram, E. & Yu, Z. Training Deep Neural Networks for the Inverse Design of Nanophotonic Structures. *ACS Photonics* **5**, 1365-1369 (2018). <https://doi.org/10.1021/acsp Photonics.7b01377>
- 29 Kanmaz, T. B., Ozturk, E., Demir, H. V. & Gunduz-Demir, C. Deep-learning-enabled electromagnetic near-field prediction and inverse design of metasurfaces. *Optica* **10**, 1373 (2023). <https://doi.org/10.1364/optica.498211>
- 30 Zhang, T. *et al.* Efficient spectrum prediction and inverse design for plasmonic waveguide systems based on artificial neural networks. *Photon. Res.* **7**, 368-380 (2019). <https://doi.org/10.1364/PRJ.7.000368>
- 31 Lee, X. Y. *et al.* Fast inverse design of microstructures via generative invariance networks. *Nature Computational Science* **1**, 229-238 (2021). <https://doi.org/10.1038/s43588-021-00045-8>
- 32 Jiang, J. & Fan, J. A. Global Optimization of Dielectric Metasurfaces Using a Physics-Driven Neural Network. *Nano Letters* **19**, 5366-5372 (2019). <https://doi.org/10.1021/acsnanolett.9b01857>
- 33 Liu, Z., Zhu, D., Rodrigues, S. P., Lee, K.-T. & Cai, W. Generative Model for the Inverse Design of Metasurfaces. *Nano Letters* **18**, 6570-6576 (2018). <https://doi.org/10.1021/acsnanolett.8b03171>
- 34 Han, X., Fan, Z., Liu, Z., Li, C. & Guo, L. J. Inverse design of metasurface optical filters using deep neural network with high degrees of freedom. *InfoMat* **3**, 432-442 (2021). <https://doi.org/10.1002/inf2.12116>
- 35 Ma, W., Cheng, F., Xu, Y., Wen, Q. & Liu, Y. Probabilistic Representation and Inverse Design of Metamaterials Based on a Deep Generative Model with Semi-Supervised Learning Strategy. *Advanced Materials* **31**, 1901111 (2019). <https://doi.org/10.1002/adma.201901111>

- 36 Wen, F., Jiang, J. & Fan, J. A. Robust Freeform Metasurface Design Based on Progressively Growing Generative Networks. *ACS Photonics* **7**, 2098-2104 (2020). <https://doi.org:10.1021/acsphotonics.0c00539>
- 37 Cao, Y. *et al.* A comprehensive survey of ai-generated content (aigc): A history of generative ai from gan to chatgpt. *arXiv preprint arXiv:2303.04226* (2023).
- 38 Ramesh, A. *et al.* in *International Conference on Machine Learning*. 8821-8831 (PMLR).
- 39 Rombach, R., Blattmann, A., Lorenz, D., Esser, P. & Ommer, B. in *Proceedings of the IEEE/CVF conference on computer vision and pattern recognition*. 10684-10695.
- 40 Cobb, P. J. Large Language Models and Generative AI, Oh My!: Archaeology in the Time of ChatGPT, Midjourney, and Beyond. *Advances in Archaeological Practice* **11**, 363-369 (2023).
- 41 Achiam, J. *et al.* GPT-4 Technical Report. *arXiv preprint arXiv:2303.08774* (2023).
- 42 Raffel, C. *et al.* Exploring the limits of transfer learning with a unified text-to-text transformer. *The Journal of Machine Learning Research* **21**, 5485-5551 (2020).
- 43 Singhal, K. *et al.* Large language models encode clinical knowledge. *Nature* **620**, 172-180 (2023). <https://doi.org:10.1038/s41586-023-06291-2>
- 44 Thirunavukarasu, A. J. *et al.* Large language models in medicine. *Nature Medicine* **29**, 1930-1940 (2023). <https://doi.org:10.1038/s41591-023-02448-8>
- 45 Boiko, D. A., Macknight, R., Kline, B. & Gomes, G. Autonomous chemical research with large language models. *Nature* **624**, 570-578 (2023). <https://doi.org:10.1038/s41586-023-06792-0>
- 46 Bastek, J.-H. & Kochmann, D. M. Inverse design of nonlinear mechanical metamaterials via video denoising diffusion models. *Nature Machine Intelligence* **5**, 1466-1475 (2023). <https://doi.org:10.1038/s42256-023-00762-x>
- 47 Dhariwal, P. & Nichol, A. Diffusion models beat gans on image synthesis. *Advances in neural information processing systems* **34**, 8780-8794 (2021).
- 48 Ho, J., Jain, A. & Abbeel, P. Denoising Diffusion Probabilistic Models. *arXiv pre-print server* (2020). <https://doi.org:None>  
arxiv:2006.11239
- 49 Song, J., Meng, C. & Ermon, S. in *International Conference on Learning Representations*.
- 50 Xiong, J. *et al.* Dynamic brain spectrum acquired by a real-time ultraspectral imaging chip with reconfigurable metasurfaces. *Optica* **9**, 461-468 (2022). <https://doi.org:10.1364/OPTICA.440013>
- 51 Rao, S., Huang, Y., Cui, K. & Li, Y. Anti-spoofing face recognition using a metasurface-based snapshot hyperspectral image sensor. *Optica* **9**, 1253-1259 (2022). <https://doi.org:10.1364/OPTICA.469653>
- 52 Wang, Z. *et al.* Single-shot on-chip spectral sensors based on photonic crystal slabs. *Nature communications* **10**, 1020 (2019).
- 53 Yang, J. *et al.* Ultraspectral Imaging Based on Metasurfaces with Freeform Shaped Meta - Atoms. *Laser & Photonics Reviews* **16**, 2100663 (2022). <https://doi.org:10.1002/lpor.202100663>

- 54 Shi, L. *et al.* Si-Based Polarizer and 1-Bit Phase-Controlled Non-Polarizing Beam Splitter-Based Integrated Metasurface for Extended Shortwave Infrared. *Nanomaterials* **13**, 2592 (2023). <https://doi.org:10.3390/nano13182592>
- 55 Dosovitskiy, A. *et al.* An image is worth 16x16 words: Transformers for image recognition at scale. *arXiv preprint arXiv:2010.11929* (2020).
- 56 Gao, L., Li, X., Liu, D., Wang, L. & Yu, Z. A Bidirectional Deep Neural Network for Accurate Silicon Color Design. *Advanced Materials* **31**, 1905467 (2019). <https://doi.org:10.1002/adma.201905467>
- 57 He, K. *et al.* in *Proceedings of the IEEE/CVF conference on computer vision and pattern recognition*. 16000-16009.
- 58 Abadi, M. *et al.* in *12th USENIX symposium on operating systems design and implementation (OSDI 16)*. 265-283.
- 59 Kingma, D. P. & Ba, J. Adam: A method for stochastic optimization. *arXiv preprint arXiv:1412.6980* (2014).

**Supplementary Document for Map Optical  
Properties to Sub-wavelength Structures Directly  
via a Diffusion Model**

Shijie Rao, Kaiyu Cui\*, Yidong Huang\*, Jiawei Yang, Yali Li, and  
Shengjin Wang, Xue Feng, Fang Liu, Wei Zhang

\* Correspondent author: [kaiyucui@tsinghua.edu.cn](mailto:kaiyucui@tsinghua.edu.cn),

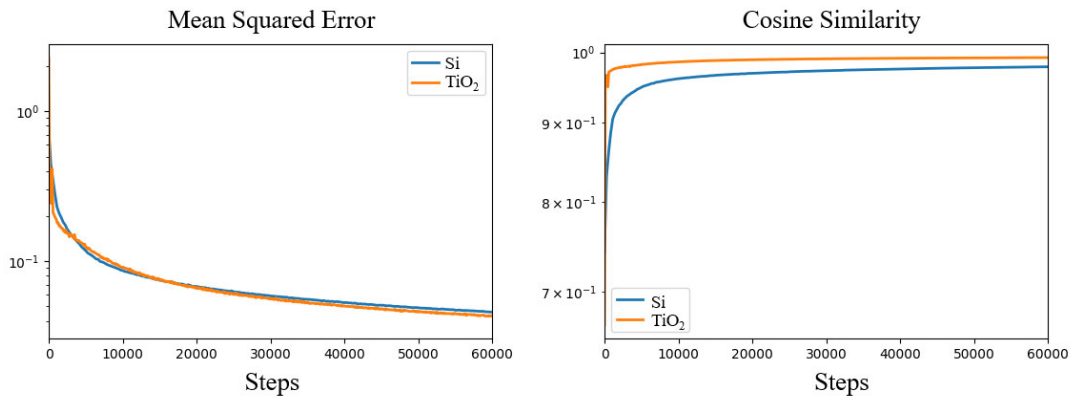
[yidonghuang@tsinghua.edu.cn](mailto:yidonghuang@tsinghua.edu.cn)

Affiliation: Department of Electronic Engineering, Beijing National  
Research Center for Information Science and Technology (BNRist),  
Tsinghua University, Beijing, China

### Supplementary Note 1. Fine-tuning the model via transfer learning.

In this work, our results are mainly based on the inverse design of 220-nanometer-thick silicon meta-atoms. Here, we take the inverse design of 600-nanometer-thick  $\text{TiO}_2$  meta-atoms as an example to demonstrate that our method can be easily converted to design meta-atoms based on other materials and other thicknesses via transfer learning. The substrate of the  $\text{TiO}_2$  meta-atoms is also  $\text{SiO}_2$ .

Our inverse design method involves four DNN models: an image encoder-decoder network, a forward prediction network, a prompt encoder network, and a latent diffusion network. Note that the image encoder-decoder network and prompt encoder network are relatively universal. We do not need to retrain them if the material or the thickness of the meta-atom changes. Only the training process of the forward prediction model requires the data acquired from a numerical simulation. During the training procedure of the latent diffusion model, the optical properties are quickly predicted by the forward prediction model, and only a dataset of 2D geometries is needed. Therefore, to convert our method to design  $\text{TiO}_2$  meta-atoms, the most important step is to fine-tune the forward prediction model.

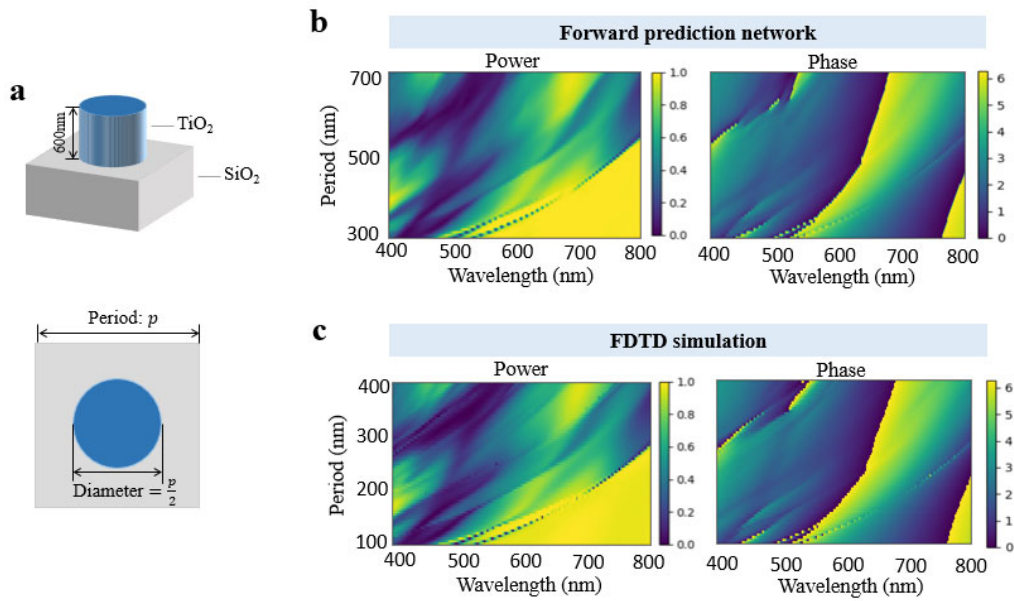


**Supplementary Fig. 1** The mean squared error and cosine similarity produced during testing.

During the training process of the forward prediction network for silicon meta-atoms, we build a training set containing  $10^5$  samples and train the network for approximately 90000 steps with a batch size of 512. To fine-tune the forward prediction



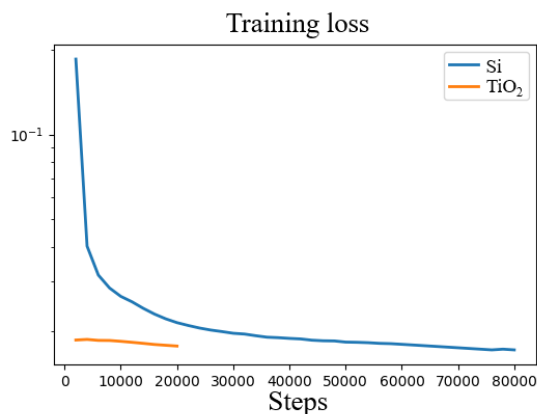
network for TiO<sub>2</sub> meta-atoms, 20000 samples are simulated for constructing the training set. Then, we fine-tune the network for 60000 steps with the same batch size. The mean squared error and cosine similarity produced on the testing set during training are shown in Supplementary Fig. 1. Through transfer learning, the forward prediction network can reach the same performance as that attained before in fewer training steps while using less training data. After the training process, the mean squared error and cosine similarity reach 0.043 and 99.22% during testing, respectively.



**Supplementary Fig. 2 Parameter sweeping results obtained for TiO<sub>2</sub> meta-atoms by the fine-tuned network. a.** The specifications of the meta-atom used for parameter sweeping. **b.** Parameter sweeping results obtained by our proposed forward prediction network. **c.** Parameter sweeping results obtained via FDTD simulation.

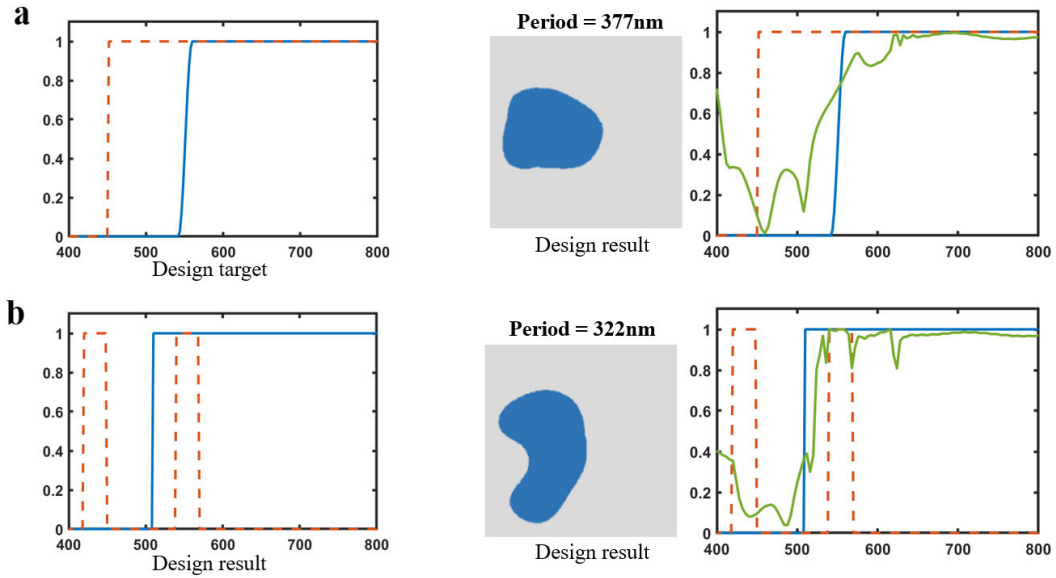
To test the performance achieved by the fine-tuned forward prediction network for TiO<sub>2</sub> meta-atoms, we also conduct a parameter sweeping task. We sweep the period of the 600-nanometer-thick TiO<sub>2</sub> cylinder meta-atom from 300 nm to 700 nm, and the diameter of the TiO<sub>2</sub> cylinder is set to half of the period, as shown in Supplementary Fig. 5a. The sweeping results obtained from our forward prediction network (Supplementary Fig. 5b) also fit well with the FDTD simulation outputs

(Supplementary Fig. 5c). These results indicate the excellent performance of our forward prediction network and the transfer learning strategy.



**Supplementary Fig. 3 Training losses induced by the latent diffusion network when inversely designing silicon and TiO<sub>2</sub> meta-atoms.**

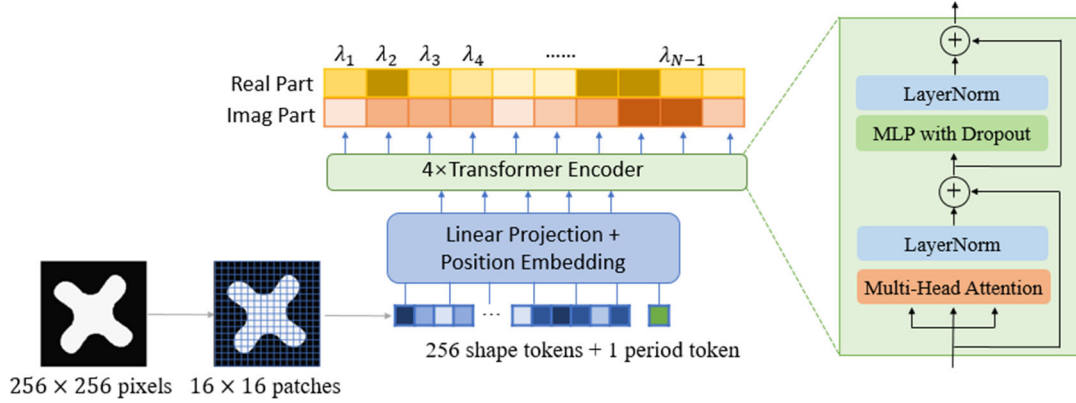
The next step is to fine-tune the latent diffusion network using the fine-tuned forward prediction network. We use the same 2D geometry dataset that we employed to train the latent diffusion network for silicon meta-atoms. The training loss is plotted in Supplementary Fig. 3. We train the original latent diffusion network for silicon meta-atoms for approximately 80,000 steps with a batch size of 128 until the loss converges. During the fine-tuning process for TiO<sub>2</sub> meta-atoms, we find that the loss converges very quickly; therefore, we stop the training procedure after 20,000 steps. Therefore, these experiments indicate that transfer learning can greatly reduce the incurred training cost.



**Supplementary Fig. 4 Inverse design examples involving  $\text{TiO}_2$  meta-atoms. a.** The inverse design results of a longwave pass filter. **b.** The inverse design results obtained with the requirements that the power transmission rate should be high at approximately 550 nm and low at approximately 430 nm.

To illustrate the inverse design capability of the fine-tuned network, several inverse design examples involving  $\text{TiO}_2$  meta-atoms are shown in Supplementary Fig. 4. These meta-atoms are generated without the  $C_4$  symmetry constraint subject to the given transmission power responses. The FDTD simulation results (green curves) of the inversely designed meta-atoms agree well with the given design targets (blue curves). The direct mapping ability of the inverse design network trained via transfer learning can be confirmed.

## Supplementary Note 2. Design of the forward prediction network.

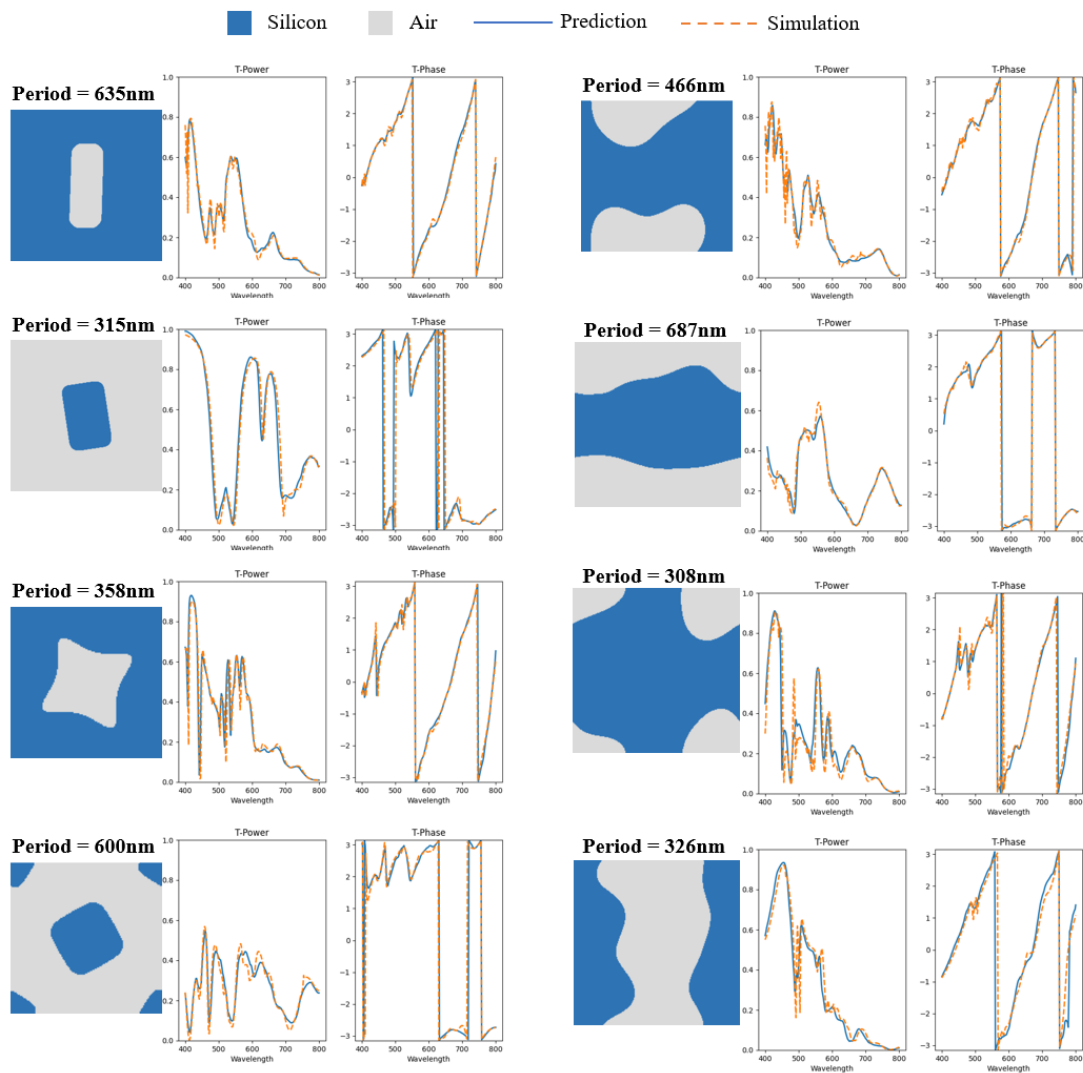


**Supplementary Fig. 5. The architecture of the transformer-based forward prediction network.**

Our forward prediction network takes the 2D geometry and period of the target meta-atom as inputs. As shown in Supplementary Fig. 5, the 2D geometry is described by a binary image with a size of  $256 \times 256$ . We slice the binary image into  $16 \times 16$  patches. Each patch contains  $16 \times 16$  pixels and is projected to a token with a feature dimensionality of 256. The period value is also projected to a token with the same dimensionality. Therefore, 256 shape tokens and 1 period token form an input feature sequence  $\mathbf{x} \in R^{257 \times 256}$ . Sinusoidal positional embeddings are then added to the feature sequence. Furthermore, the feature sequence is processed by 4 transformer encoder<sup>1</sup> blocks. Each block has 8 heads, and the head size is set to 256. In this way, the output sequence  $\mathbf{y} \in R^{257 \times 256}$  has 257 tokens with a dimensionality of 256. Finally, each output token is mapped to a vector with 2 dimensions by another linear projection, and we can obtain the final sequence  $\mathbf{z} \in R^{257 \times 2}$ . The first dimension of  $\mathbf{z}$  indicates 257 sample points with wavelengths from 400 nm to 800 nm, and the second dimension contains the real and imaginary parts of the transmission response. The network is trained by the Adam<sup>2</sup> optimizer with a batch size of 512 for 320 epochs. The learning rate is set to 0.0002, and the weight decay rate is set to 0.0001.

### Supplementary Note 3. Performance of the forward prediction network.

According to our quantitative analysis, the mean squared error and cosine similarity of our forward prediction network reach 0.040 and 98.2%, respectively. Our forward prediction network requires approximately 42 ms on an Intel Core i7-11700 CPU @ 2.5 GHz and approximately 1.4 ms on an NVIDIA RTX 2080Ti GPU, while the FDTD simulation requires approximately 70 s on average on the same CPU. Our network, which is powered by a GPU, can operate 50000 times faster than the FDTD simulation.

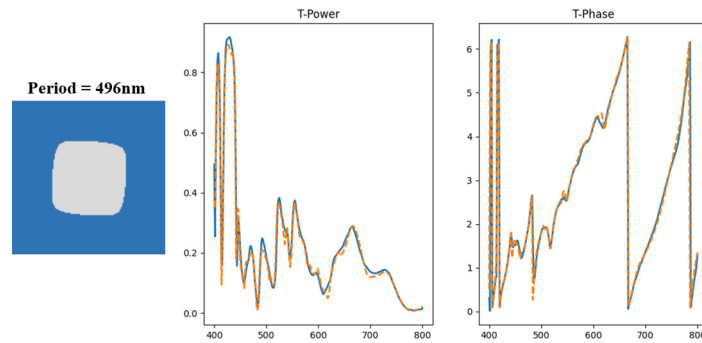


**Supplementary Fig. 6 Visualization results produced by the forward prediction network.**

A more intuitive visualization of the results is shown in Supplementary Fig. 6. We

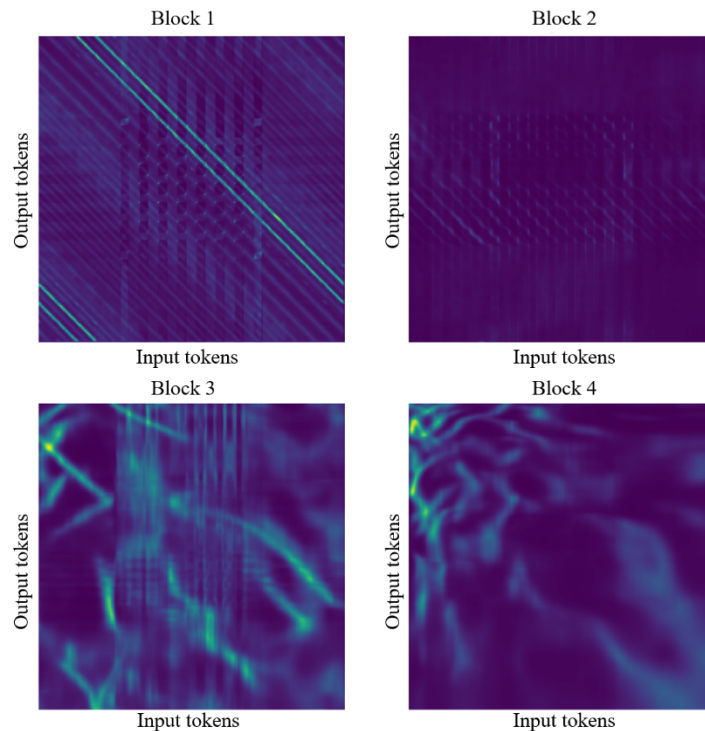
randomly select some samples from the testing set. These meta-atoms include rectangular pillars, rectangular holes, C4 symmetric pillars, C4 symmetric holes, and some randomly shaped structures. The incident light is set to horizontal polarization. The predicted transmission responses match well with the FDTD simulation outputs. These results illustrate that our forward prediction network can greatly accelerate the forward prediction process while maintaining acceptable prediction error. This acceleration is vital for effectively training the latent diffusion network.

**Supplementary Note 4. Analysis of the attention maps produced by the forward prediction network.**



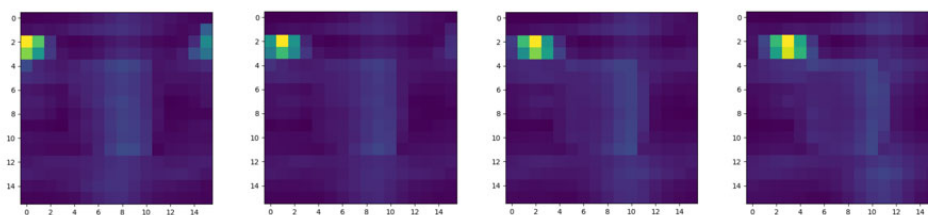
**Supplementary Fig. 7 The meta-atom used for analyzing the attention maps of the forward prediction network.**

We choose a random meta-atom as an example to analyze the attention maps yielded by the forward prediction network and try to understand what the network has learned to accurately predict the transmission response. The meta-atom is shown in Supplementary Fig. 7. The prediction results (blue curves) obtained for the transmission power and phase response highly match the FDTD simulation results (orange dashed curves).



**Supplementary Fig. 8 The attention maps of the four transformer blocks.**

Four transformer encoder blocks are contained in our forward prediction network, and each block generates an attention map that maps the input tokens to the output tokens via a self-attention mechanism. The generated attention maps are shown in Supplementary Fig. 8. During the test, we find that the first two attention maps are relatively stable under different inputs, while the last two attention maps are highly related to the input data.



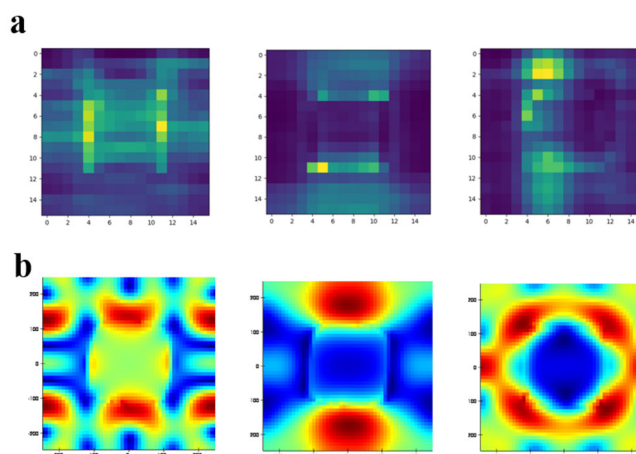
**Supplementary Fig. 9 The reshaped attention weights of the first four rows from the attention map of block 1.**

The attention map of block 1 can be effectively interpreted because the input tokens have clear physical meanings. The first 256 tokens correspond to the 256 image patches, and the last token represents the period. We can reshape the first 256 attention weights of each row of the attention map to a  $16 \times 16$  matrix. Some of the results are displayed in Supplementary Fig. 9 and indicate that the first transformer encoder block mainly extracts features from the spatially adjacent patches. This is understandable because light fields are usually localized in these subwavelength dielectric structures, and the light field of each patch highly depends on its neighboring patches because these patches can provide boundary conditions. This is similar to the FDTD simulation output, where at every time step, the electrical field of each cell is calculated from the magnetic fields of the neighboring cells.

The attention map of block 2 can also be interpreted. As the output tokens of block 1, which are also the input tokens of block 2, come from the adjacent patches, we can still assume that each input token of block 2 correlates to one of the  $16 \times 16$  spatial locations. Therefore, for the attention map of block 2, we can also reshape the first 256



attention weights in each row to a  $16 \times 16$  matrix (Supplementary Fig. 10a). Different from the results of block 1, these results show that each output token of block 2 no longer only depends on the adjacent patches but is calculated from a relatively global feature. Each output token represents a different global feature. This can be attributed to block 2 mainly analyzing the nonlocal light field. We find that the visualized attention weight matrix (Supplementary Fig. 10a) exhibits some similarities to the electrical field distribution produced at different wavelengths for the meta-atom simulated by FDTD (Supplementary Fig. 10b). Therefore, we can assume that block 2 tries to predict the global light field distribution at each wavelength, which is important to the transmission response.



**Supplementary Fig. 10.** **a.** The reshaped attention weights of some rows from the attention map of block 2. **b.** The distributions of the electrical fields inside the meta-atoms simulated by FDTD at different wavelengths.

The attention maps of blocks 3 and 4 are less interpretable because we cannot find a clear physical explanation for each token. The output tokens of block 2, which are also the input tokens of block 3, no longer have a one-to-one correspondence with one of the  $16 \times 16$  spatial locations. Instead, each token represents a high-level abstract feature, and finally, the tokens are transformed from the spatial domain to the spectral domain because each output token of block 4 is bound to a certain wavelength. This domain transfer task is mainly accomplished by block 4. The role of block 3 may be to map the local and nonlocal light fields to the desired optical properties.

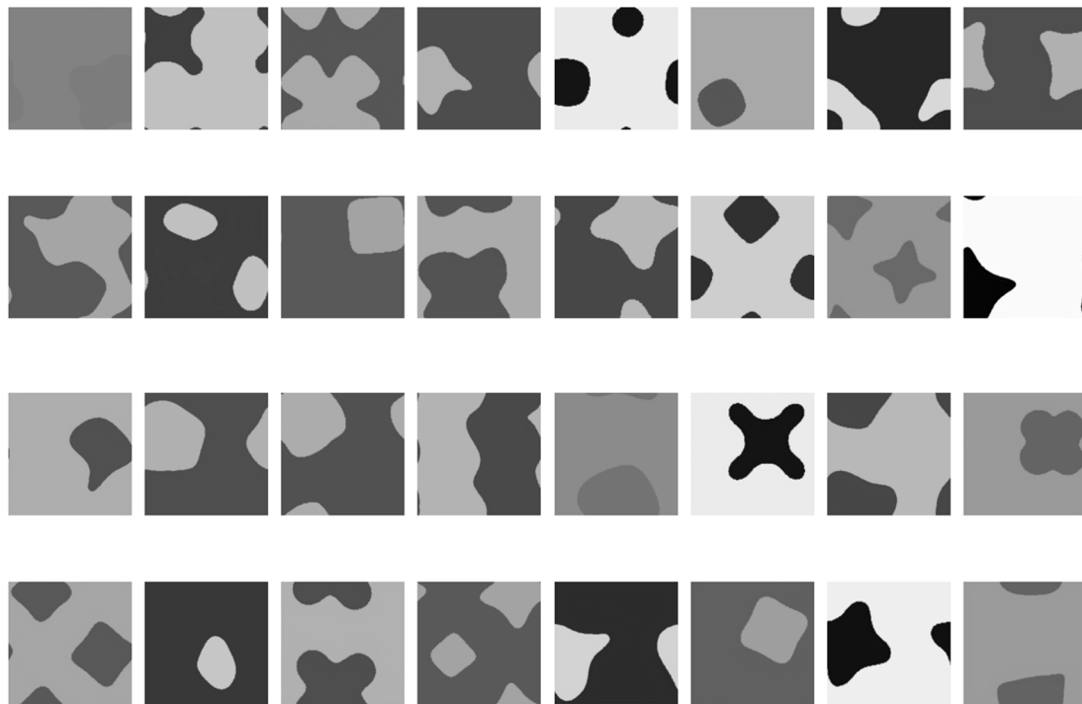
## **Supplementary Note 5. Implementation details of the prompt encoder network.**

Our prompt encoder network is implemented by the same transformer encoder block shown in Supplementary Fig. 5. The encoder network has 4 transformer encoder blocks with 4 heads, and the head size is set to 128. An additional decoder network is also designed to train the encoder network. The decoder network has 2 transformer encoder blocks with 4 heads, and the head size is 64. The inputs of the prompt encoder network are the property vector (the transmission power spectrum, transmission phase spectrum, or complex-valued transmission spectrum) and the property mask. Every element of the property vector is regarded as an input token of the transformer encoder. All of the tokens in the masked bands (where  $mask = 0$ ) are replaced by the same trainable masked token. Sinusoidal positional embeddings are also added to the input tokens.

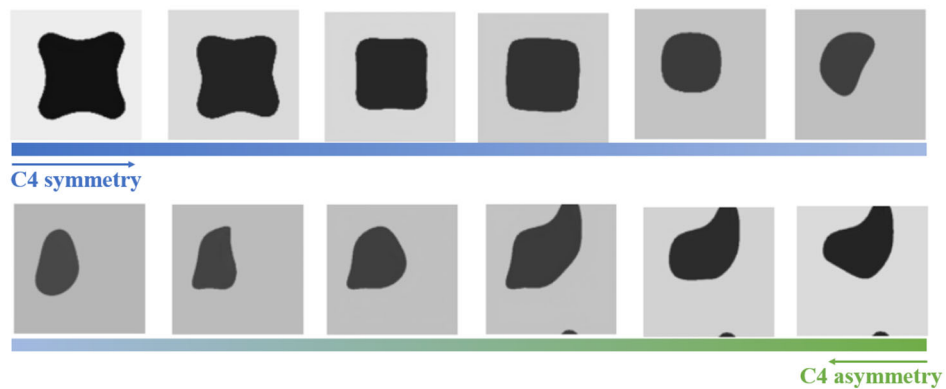
During training, masks are randomly generated and dropped with a dropout rate of 0.3. If a mask is dropped, it is set to all ones, and none of the input tokens are replaced by the masked token. The training data are acquired from the simulated meta-atom dataset used to train the forward prediction network. We train the networks with a batch size of 512 for 25000 steps. The Adam optimizer is also adopted to train the network. After training, the prompt decoder network is discarded, and the prompt encoder network is utilized to train the latent diffusion network.

**Supplementary Note 6. Additional inverse design results provided by the diffusion network.**

First, to demonstrate the generative capabilities of our latent diffusion network, some results that are randomly generated without any conditional inputs are shown in Supplementary Fig. 11. The darker region represents air, the lighter region represents dielectric, and the degree of darkness represents the period of the meta-atom. Our latent diffusion network can generate various shapes with and without C4 symmetry.

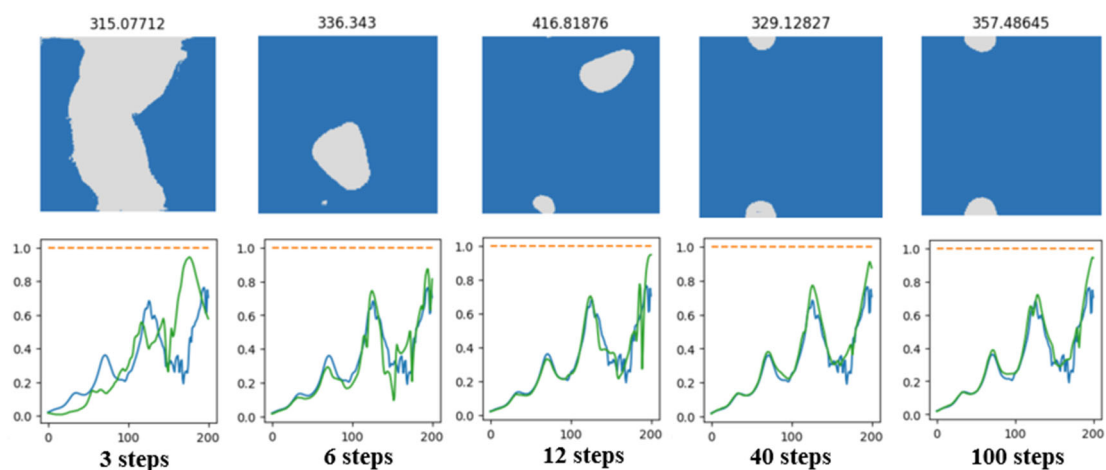


**Supplementary Fig. 11** The shapes randomly generated by the latent diffusion network.



**Supplementary Fig. 12** The interpolated shapes between a C4 symmetric shape and a C4 asymmetric shape generated by a latent diffusion network.

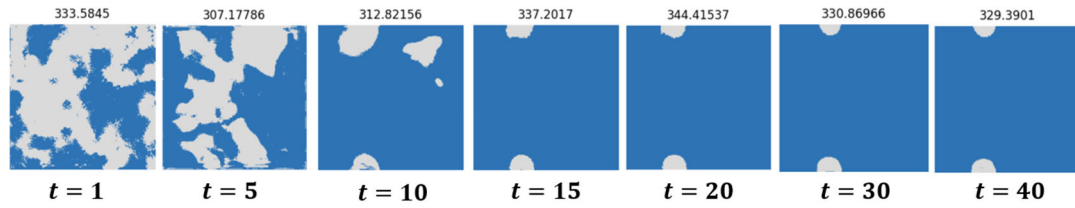
By proceeding through the latent space, we can see how the diffusion network utilizes interpolation to generate new shapes. We choose an initial noise value  $n_1$  that can generate a C4 symmetric shape and another initial noise value  $n_2$  that can generate a C4 asymmetric shape and employ the latent diffusion network to generate shapes using linear interpolations between  $n_1$  and  $n_2$ . The interpolated shapes are shown in Supplementary Fig. 12. Diffusion models have powerful abilities to model images from different domains. The results show that our latent diffusion network can establish a method for interpolating between C4 symmetric and C4 asymmetric shapes, thus generating new shapes that are not included in the training set. This ability to generate new shapes can greatly enlarge the search space.



**Supplementary Fig. 13 Inverse design results obtained using different numbers of diffusion steps.**

The number of diffusion steps is an important hyperparameter in diffusion models. As we adopt a continuous diffusion time to train the network, the number of diffusion steps  $N$  can be dynamically changed during inference. A larger  $N$  indicates a more refined denoising process. We conduct the same inverse design task as that shown in Fig. 4c but change  $N$  to different values (the results shown in Fig. 4c are generated under  $N = 40$ ). The inverse design results obtained under different  $N$  values are shown in Supplementary Fig. 13. The first row shows the generated meta-atoms with their periods, and the second row shows the corresponding design targets (blue curves), input masks (orange curves), and design results (green curves). The results show that

when  $N = 6$ , the inverse design result starts to satisfy the imposed requirement. When  $N = 12$ , we can obtain a relatively reliable inverse design result. When  $N \geq 40$ , the inverse design result starts to converge. Our latent diffusion network can effectively obtain inverse design results with few denoising steps. Then, we set  $N = 40$ , and we can see how the diffusion network denoises the initial random noise to form the desired output. This denoising process is shown in Supplementary Fig. 14.



**Supplementary Fig. 14 Denoising process of the diffusion network.**

## References

- 1 Vaswani, A. *et al.* Attention is all you need. *Advances in neural information processing systems* **30** (2017).
- 2 Kingma, D. P. & Ba, J. Adam: A method for stochastic optimization. *arXiv preprint arXiv:1412.6980* (2014).